Available online at www.sciencedirect.com

ScienceDirect

Proceedings of the Combustion Institute 36 (2017) 1001–1009

Proceedings of the Combustion Institute

www.elsevier.com/locate/proci

Soot particle size distributions in premixed stretch-stabilized flat ethylene–oxygen–argon flames

Joaquin Camacho [a], Ajay V. Singh [a], Weijing Wang [b], Ruiqin Shan [c], Edward K.Y. Yapp [c], Dongping Chen [a], Markus Kraft [a,b], Hai Wang [a,*]

[a] *Mechanical Engineering Department, Stanford University, Stanford, California 94305-3032, USA*
[b] *School of Chemical and Biomedical Engineering, Nanyang Technological University, Singapore 637459, Singapore*
[c] *Department of Chemical Engineering and Biotechnology, University of Cambridge, Cambridge CB2 3RA, UK*

Received 4 December 2015; accepted 27 June 2016
Available online 7 July 2016

Abstract

Evolution of particle size distribution function (PSDF) was studied in premixed stretch-stabilized flat flames for the first time. The purpose is to demonstrate that stretch-stabilized flames can broaden the experimental flame condition space for studying soot formation in a pseudo-one dimensional flow configuration. PSDFs were measured in three series of atmospheric-pressure ethylene–oxygen–argon flames with maximum temperatures around 1980, 2000, and 2160 K. The measured PSDFs show a strong effect of flame temperature as nucleation and growth of soot is found to be suppressed towards high temperatures. Simulations using a population balance soot model show reasonably good agreement with the 1980 and 2000 K series of flames, but it significantly overpredicts the number density and size of soot in the highest temperature flame. Numerical tests suggest that the discrepancy can be caused by high-temperature reversibility in surface growth and other processes.

© 2016 The Combustion Institute. Published by Elsevier Inc. All rights reserved.

Keywords: Soot; Laminar flame; Particle size distribution; Modeling

---

1. Introduction

It is well known that soot formation is greatly impacted by thermodynamic reversibility towards high temperatures. This reversibility causes soot yield to follow a rise-then-fall behavior or bell-shaped dependency with respect to temperature in shock tubes [1–3] and flames [4–7]. At a detailed level, the kinetic causes for the reversibility of polycyclic aromatic hydrocarbon (PAH) formation and growth have been discussed some time ago [8,9]. For soot nucleation and size growth involving PAH clustering, PAH condensation and particle–particle coagulation, the importance of microscopic reversibility has been also discussed (see, e.g., [10–16]). More recently, detailed modeling of soot formation has generally considered the reversibility of soot particle nucleation and coagulation in the form of a stick probability (see,

---

[*] Corresponding author. Tel.: +650 497 0433; Fax: +1 650 723 1748.
E-mail address: haiwang@stanford.edu (H. Wang).

http://dx.doi.org/10.1016/j.proci.2016.06.170
1540-7489 © 2016 The Combustion Institute. Published by Elsevier Inc. All rights reserved.

e.g., [12,14,15,17,18]), which is expected to be dependent on size, temperature and pressure. Physical and quantitative understanding of these dependencies is currently lacking. In particular, reversibility is amplified at high temperatures (>2000 K) yet experimental observations in flames with low-dimensional flow geometry (e.g., the McKenna type burner) above this temperature have proven to be difficult for reasons to be discussed below.

Previously we have shown that the burner-stabilized stagnation flame (BSSF) approach coupled with mobility sizing can yield a wealth of information about the competition between various soot growth processes [19–21]. The approach allows for the evolution of the soot particle size distribution function (PSDF) to be followed quite closely while reducing the problem of probe perturbation and ill-defined boundary conditions [21,22]. The data generated have been useful to model development and comparison (see, e.g., [14,18,23,24]). However, the BSSF approach has limitations. Fundamentally, flame stabilization is achieved through heat loss to the burner in burner-stabilized flames, thus it is generally difficult to access high temperature flames (>2000 K) where the effect of thermodynamic reversibility is expected to be amplified. High temperature flames also hasten non-uniform porosity changes in the porous plug thus creating a non-uniform radial velocity profile after some period of measurement – an experimental issue that would impact data quality [21]. This porosity change problem is further exacerbated in experiments for liquid fuels as keeping the fuel in a vaporized state usually requires heating of the porous plug. In addition to porosity changes, the elevated temperature increases heterogeneous reaction rates in the porous plug, which can lead to coking and changes in the composition of the unburned gas due to fuel cracking.

For reasons discussed above, it would be beneficial to develop a new burner that would remove the aforementioned problem and still allow for particle size distributions to be followed in a one-dimensional or quasi-one-dimensional flame system. In this work, we show that premixed stagnation flat flames offer this alternative configuration and demonstrate that such flames can be used to extend the experimental range for studying nascent soot formation through mobility sizing, while still maintaining well defined boundary conditions in a pseudo-one dimensional geometry. The so-called stationary premixed planar flame in stagnation flow (alternatively known as a stagnation flame or premixed stretch-stabilized flat flame) is commonly used to examine fundamental combustion phenomena like flame speed and extinction [25]. Stretch-stabilized flat flames have certain advantages over burner-stabilized flames. The flame stabilization mechanism of stretch-stabilized flames is based on flow stretch rather than heat loss. For this reason, stretch-stabilized flat flames have maximum flame temperatures, $T_{f,\max}$, approaching the adiabatic flame temperature, and in many cases exceeding the adiabatic flame temperature due to Lewis number effects [25]. Studies of low-vapor pressure, liquid fuels become significantly more reliable because stretch-stabilized flat flames are issued from a simple nozzle. In this work, experimental observations of the PSDF in a series of ethylene–oxygen–argon flames are compared to predictions from a population balance model. Relatively high flame temperatures are accessed with stretch-stabilized flat flames to assess the accuracy of a soot model against the measurement.

2. Experimental

The experimental setup, summarized in Fig. 1, consists of a burner with an aerodynamically shaped nozzle, a stagnation surface/sampling probe assembly and a scanning mobility particle sizer (SMPS). The aerodynamic shape of the burner nozzle body is designed to achieve plug flow at the burner exit (1.43 cm nozzle exit diameter). The distance between the burner nozzle and stagnation surface, L, is held constant at 1.0 cm. The standing distance between the flame and stagnation surface/sampling probe, L_s, may be varied by changing the unburned gas flow rate.

Flame sample was drawn into a micro-orifice (127 μm diameter, 125 μm wall thickness) embedded within and flush to the stagnation surface on a water-cooled aluminum disc. The techniques for sampling and dilution ratio calibration (based on CO_2 concentration measurement) are identical to our earlier work [21]. Figure S1 of the Supplemental material shows the dilution ratio calibration for the current stretch-stabilized flame. An optimum dilution ratio was established in accordance with previously established procedures [21,26,27]. The PSDF was determined in terms of mobility diameter as measured by the TSI SMPS (models and settings found in [19]) with previously described mobility diameter corrections [28,29].

The gas temperature at the nozzle exit, T_n, was measured with an uncoated fine-wire (125 μm wire diameter) Pt–Rh thermocouple placed near the centerline of the flow. Similar to the BSS flame sampling technique [19], the stagnation surface doubles as a sampling probe. The temperature at the stagnation surface, T_s, was measured by a type-R thermocouple (0.2 cm wire diameter) placed flush with the surface such that the bead is exposed to the sample gas 1 cm away from the centerline of the flame. The gas temperature at the nozzle exit was determined to be $T_n = 347 \pm 10$ K; and the stagnation surface temperature was $T_s = 385 \pm 25$ K. The uncertainty values quoted here are one standard deviation across all flames studied. Numerical sensitivity calculations show that within the uncertainty values quoted the flame structure exhibits

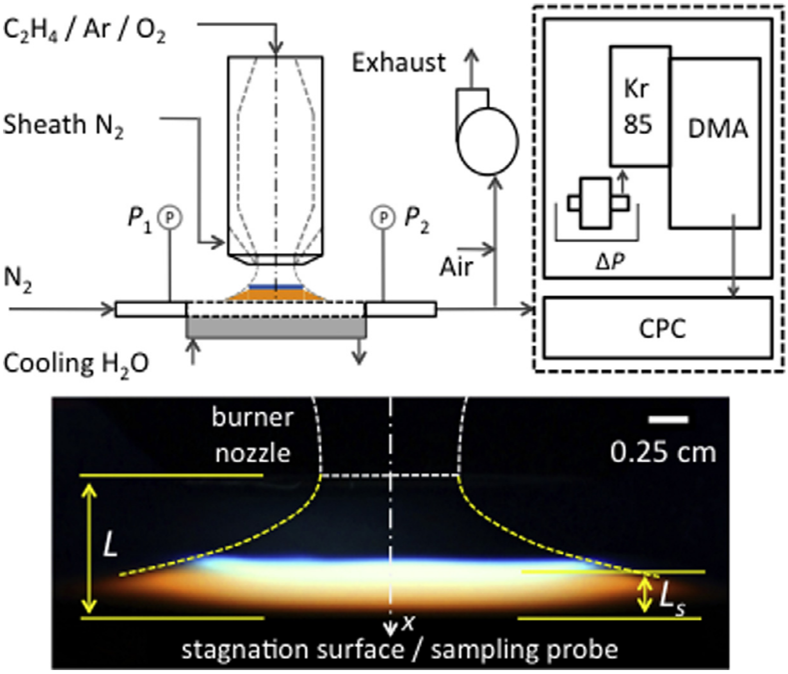

Fig. 1. Experimental setup and image of a typical flame.

Table 1
Flame parameters[a] and lognormal distribution parameters measured for the large particle-size mode.

Flame No	Velocity[b] v_0 (cm/s)	Global strain rate a (s^{-1})	Standing distance[c,d] L_s (cm)	$T_{f,max}$[d] (K)	$t_p(L)$ (ms)	$N_2 \times 10^{-10}$ (cm^{-3})	$\sigma_{g,2}$	$\langle D_m \rangle_2$ (nm)
S1 series: 12.7% C_2H_4/15.8% O_2/71.5% Ar ($T_{ad}=1886$ K)								
A	50.9	58.6	0.36	1992	8.8	9.1	1.36	5.8
B	45.2	52.0	0.40	1977	9.7	8.4	1.42	6.8
C	39.7	45.7	0.44	1977	10.6	6.0	1.43	8.8
D	31.3	36.0	0.55	1972	11.9	3.5	1.54	13.7
S2 series: 13.2% C_2H_4/16.5% O_2/70.3% Ar ($T_{ad}=1947$ K)								
A	66.0	76.0	0.32	1996	7.0	7.7	1.31	3.9
B	57.1	65.7	0.36	2006	7.8	7.5	1.32	5.0
C	45.8	52.7	0.44	2015	9.2	6.7	1.34	5.8
D	33.1	38.1	0.56	2023	10.6	4.9	1.45	10.0
S3 series: 15.6% C_2H_4/19.5% O_2/65.0% Ar ($T_{ad}=2103$ K)								
A	110.0	126.6	0.34	2155	4.1	0.5	1.12	3.9
B	77.2	88.9	0.45	2169	5.4	1.5	1.13	4.3
C	57.5	66.2	0.56	2163	6.4	1.0	1.13	4.6

[a] All unburned mixtures have the equivalence ratio equal to 2.4. Nozzle-to-stagnation surface separation (L) is 1 cm.
[b] Unburned gas velocity at 298 K and 1 atm. Sheath N_2 velocity for each flame is v_0.
[c] Distance from the stagnation surface to position of maximum flame temperature.
[d] Computed using OPPDIF and USC Mech II with $T_n=343$ K and $T_s=395$ K.

little sensitivity towards the boundary temperature variations.

The evolution of the PSDF was determined for three series of ethylene–oxygen–argon flames. The unburned gas composition and cold gas velocity are summarized in Table 1 for each series. The maximum flame temperatures computed using OPPDIF and USC Mech II (to be discussed later) are around 1980, 2010 and 2160 K for flame series S1–S3, respectively. In each series, the variation in unburned gas velocity has the effect of changing the flame standoff distance by altering the kinematic balance between the local flame speed and the normal flow velocity immediately upstream of the flame surface [25]. The examined flames range from relatively high velocity flames approaching the limit where stretch-induced flame extinction processes occur to low velocity flames approaching the flashback limit. For each series of flames, the evolution of the PSDF was observed as a function of flame standoff distance. The nitrogen sheath flow velocity is matched to the cold gas velocity for each flame because the flame edges can be impacted for high sheath flow rates (see Figure S2 of the Supplemental material).

The position of the flame was also determined experimentally by flame luminosity. A Canon Rebel T5i DSLR was used with a shutter speed of 1/20 s and field of view of 12 cm × 8 cm. The position was calibrated by averaging 4 images of a ruler to obtain the pixel per millimeter count in the field of view. To account for slight flame oscillation, 140 flame images were processed and averaged. The luminosity was determined as a function of axial and radial position and a Sobel edge detection algorithm [30] in ImageJ was used to detect the edges of the blue flame zone.

3. Computational

The stochastic soot model was previously applied to model soot formation in laminar premixed flames [28,31]. For the current flames, a modified OPPDIF [23,32] code was used to compute the gas-phase species profiles, including PAH concentrations as derived from the ABF model [33] which is based on the model described in Wang and Frenklach [34] with additional PAH growth reactions. The ABF model has been shown to over-predict the laminar flame speed of ethylene flames which makes the predicted flame temperature lower than observed in BSS flames [23]. To address this limitation, the temperature profile was obtained first from computations using USC Mech II [35] and then imposed onto the ABF model computations. The boundary conditions for the energy equation were given by the measured temperatures at the nozzle exit and the stagnation surface/sampling probe. The stochastic model of soot formation was then applied as a post processing step where the imposed temperature and computed species profiles were supplied as input. The net molar rate of production of pyrene was used to determine the rate at which pyrene monomers are "inserted" into the soot model particle ensemble.

The stagnation flow field was simplified by invoking the pseudo one-dimensional formulation [36,37]. Plug flow is designated at the burner boundary and non-slip conditions are assumed at the stagnation surface boundary. The net diffusive velocity at the stagnation surface is zero due to balancing thermal diffusion and Fickian processes. Probe sampling effects such as the flow field perturbation due to the finite velocity at the stagnation surface were not accounted for. The relevant species profiles were expressed in terms of the residence time of a Langrangian particle traveling from the burner to the stagnation surface by considering the axial convective and thermophoretic velocities [19,23].

The soot model assumes spherical particles and pyrene dimerization as the inception step, particle–particle coagulation, surface growth by H-abstraction-C_2H_2 addition, PAH (pyrene) condensation and oxidation by O_2 and OH [33]. The reaction steric factor, as given in [33], is applied to the overall surface growth rate

The collision rates are determined by a transition-regime coagulation kernel [38]. The computed particle diameter is compared to mobility diameter, although the particles as small as those sampled here may not be spherical [21].

4. Results and discussion

We first discuss the key characteristics of the stagnation planar flames studied herein. Numerical solution of selected major and minor species of Flame S2b is shown in Fig. 2. As a typical representation of the structure for the stretch-stabilized flames studied, the preheat zone of the flame is not attached to the burner. Rather, the rise in

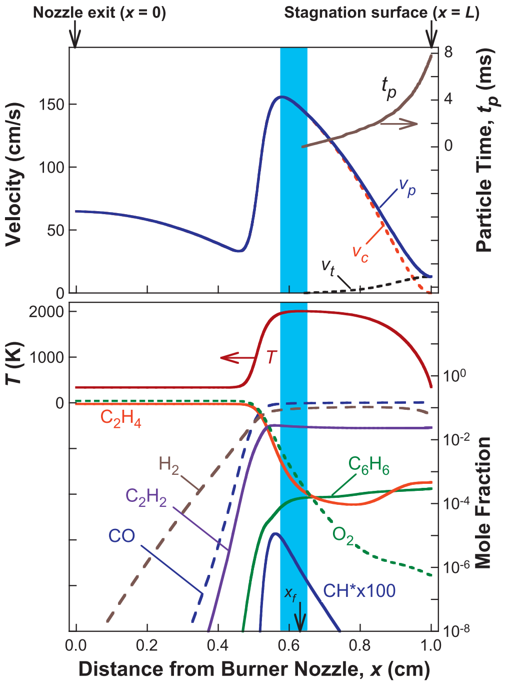

Fig. 2. Profiles of temperature, species mole fraction, velocity (the total velocity $v_p = v_c + v_t$, where v_c is the convective velocity of the gas and v_t is the thermophoretic velocity of the particle, and particle time t_p computed for Flame S2b. The band indicates the observed location of the blue flame. x_f indicates the position of maximum flame temperature.

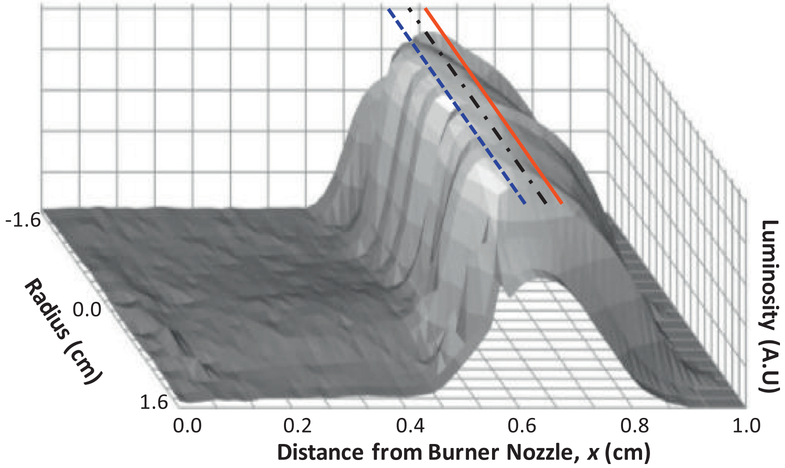

Fig. 3. Measured flame luminosity as a function of axial and radial position for Flame S3a. Lines: computed location of the peak CH* concentration (dashed line), the location of the peak flame temperature (solid line) and the midpoint of the measured edges of the blue flame zone (dash-dotted-dash line).

temperature occurs where the local flow velocity approaches the laminar flame speed of the underlying mixture [25]. Markers for the flame location can be taken as the chemiluminescence zone or the location of the peak flame temperature with varying degrees of overlap reported between the two [39,40]. The measured luminosity of Flame S3a is shown in Fig. 3. A straight luminosity plateau region is observed and this may result from a combination of line of sight superposition, contributions from multiple chemiluminescent species and soot radiation [40]. The blue zone location was measured by detecting the edges with the Sobel algorithm. The locations of the computed peak CH* concentration, peak flame temperature, and midpoint of the measured blue zone edges fall within the region of peak luminosity observed.

As shown in Fig. 2, the observed chemiluminescence zone is also close to the CH* production zone and region of maximum flame temperature computed for the centerline of Flame S2b. For all flames studied, the average of the measured flame edges consistently falls within 200 and 400 μm of the computed peak temperature and CH* concentration, respectively, with the average edge location falling somewhat downstream of the computed CH* peak. Kojima et al. [40] reported that the CH* peak detected experimentally in the planar region of premixed fuel-rich slot flames also occurs 200 μm after the peak value. With the above consideration, the agreement between the measured flame position and the computed flame structure is deemed reasonable. Furthermore, the plug flow boundary condition assumed for the unburned gas in OPPDIF calculation is appropriate.

The variation in the unburned gas velocity corresponds to changes in the global strain rate of the flame, $a = v_0(T_n)/L$, where $v_0(T_n)$ is the unburned gas velocity at the nozzle exit, which in turn causes the flame standing distance and the particle time to vary within each series of the flame (Table 1). For illustrative purposes we assume that particle time zero starts at the maximum flame temperature, and the particle time may be calculated by integrating the inverse of particle velocity, v_p, from the maximum flame position, x_f, i.e., $\int_{x_f}^{L} dx/v_p$, where v_p is a sum of the convective velocity, v_c, and particle thermophoretic velocity, v_t, approximated from the Waldmann theory [41]. As an example, Fig. 2 shows profiles of these velocity terms for Flame S2b. The total particle time, $t_p(L)$, is the time for which a particle traverses from x_f to L, where the soot PSDF is measured. This time is 12 ms or shorter, as shown in Table 1.

Qualitatively the observed soot PSDFs are similar to those measured in ethylene BSSF previously (see, e.g., [21,42]), as shown in Fig. 4 for series S1 and S2 flames and Fig. 5 for series S3 flames. For the lowest temperature flame studied (S1, ~1980 K), the soot number concentration N exhibits mostly a bimodal distribution with respect to the mobility diameter D_m. Within the range of particle size that can be detected, the PSDF evolves to mostly an apparent unimodal distribution for flames at ~2010 K (series S2). Soot measured in series S3 flames with $T_{f,\max} \sim 2160$ K is relatively small and an apparent unimodal distribution is observed. In all cases, however, the PSDF may be characterized by a bi-lognormal distribution function (see, e.g., [42]) consisting of a geometric

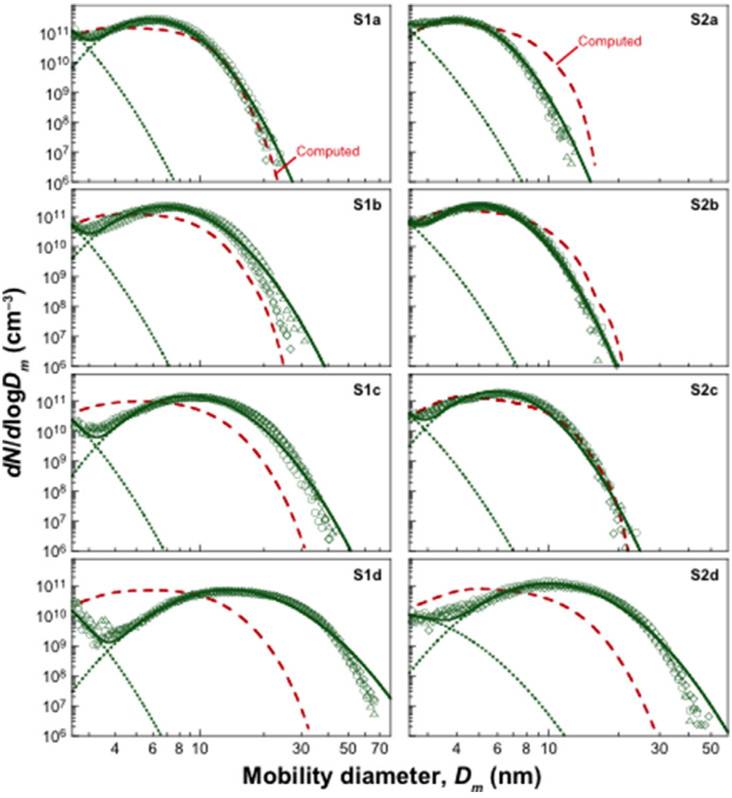

Fig. 4. Particle size distributions of series S1 and S2 flames. Symbols: experimental data (different symbols from repeated runs, showing data reproducibility); solid and dotted lines: fits using bi-lognormal distribution function; dashed line: computed using the population balance model.

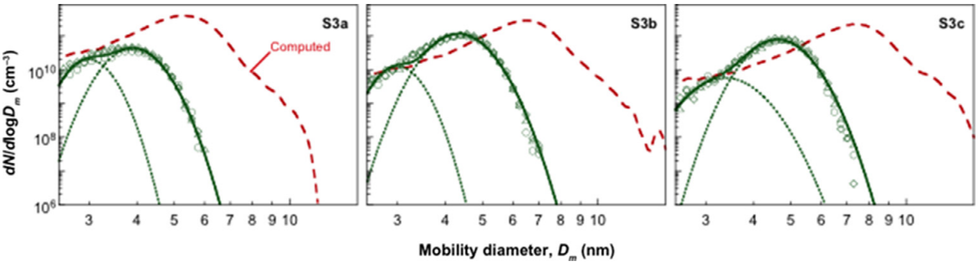

Fig. 5. Particle size distributions of series S3 flames. Symbols: experimental data (different symbols from repeated runs, showing data reproducibility); solid and dotted lines: fits using bi-lognormal distribution function; dashed line: computed using the population balance model.

standard deviation σ_g and median diameter $\langle D_m \rangle$ for each mode. Fits to each mode can be seen as the dotted lines in Figs. 4 and 5, while the fit to the entire distribution function are represented by the solid line. Due to limited data resolution in the small size range, only the large-size mode ($i = 2$) parameters are listed in Table 1. For each series of flames, the evolution in distribution number density, median particle diameter and geometric standard deviation are largely governed by particle–particle coagulation processes. As shown in Table 1, the distribution number density decreases as the particle time increases for each series of flames. The decrease in the number density is accompanied with an increase in the geometric standard deviation and the median particle size. Production of soot decreases from series S1–S3 as the flame temperature increases and particle time decreases at the same time. The decreasing particle time is not, however, the cause of soot diminishment as will be discussed below.

Also shown in Fig. 4 are the ABF model predictions. The agreement for S1a and S2a flame is remarkably good. For other flames, the agreement is less than satisfactory. The model tends to underpredict the size growth rate towards longer particle times as compared to the experiment. The problem may lie in the spherical particle model assumption which impacts both the surface growth rate and the mismatch between mobility and spherical-equivalent diameters. Recent helium ion microscopy studies [43–45] and investigations into the mass/mobility size relationship [21] have shown that nascent soot particles can deviate from spherical morphology even at the very early growth stages.

For series S3 flames, ($T_{f,\mathrm{max}} \sim 2160$ K, Fig. 5) the model drastically overpredicts the particle formation and growth both in particle number concentration and size. Specifically, the computed number density is larger than the measured values by up to 5 times and the computed particle size can be twice that of the experimental value. Overall the volume fractions are over-predicted by an order of magnitude for all three flames in series S3.

Numerical sensitivity analyses were carried out here to shed light on the above discrepancy. Selected results are presented here. A complete account of these analyses can be found in the supplemental material. We expect that the effect of thermodynamic reversibility can exhibit in all nearly all fundamental sooting processes, including particle inception, coagulation, PAH condensation and surface growth reactions. Thus, the influence of a non-unity sticking probability (see, e.g., [16,28] for particle–particle coagulation, PAH condensation and pyrene dimerization leading to particle inception is examined by reducing the respective sticking probabilities to 0.01. The results are shown in Fig. 6 for Flame S3c as an example. More thorough results are provided in the Supplemental material. Reduced coagulation and pyrene dimerization rates lead to large changes in the PSDF for this and all flames studied (see, Figs. S3–S5). It is tempting to fit these stick probability values to the available PSDF profiles but the inherent, complex coupling among the particle processes along with the kinetic uncertainty in pyrene concentration predictions across the flames renders this a highly over-simplified approach.

Non-unity sticking probability has been discussed earlier [16]. Saggese et al. [18] proposed a particle size-dependent sticking probability expression and used it to model the PSDFs in a burner stabilized ethylene flame [21]. A test using the same sticking probability expression shows less than satisfactory result, as seen by comparing curve (2) of Fig. 7 with the experimental data and base case cal-

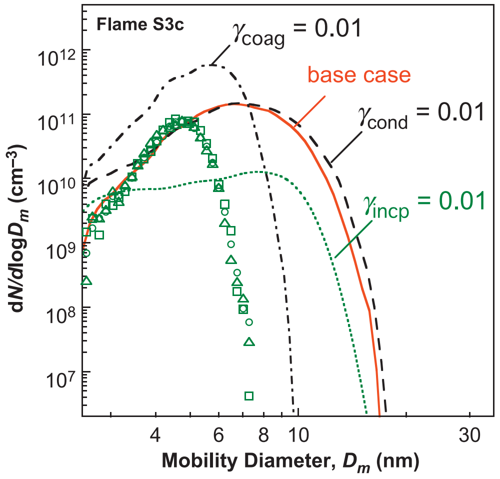

Fig. 6. Sensitivities of PSDF to the efficiencies of particle inception, particle–particle coagulation and PAH (pyrene) condensation computed for Flame S3c. Symbols: experimental; lines: computed.

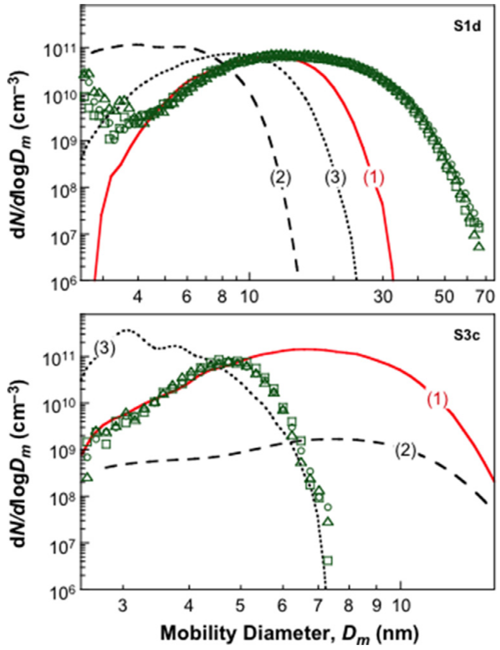

Fig. 7. Sensitivities of PSDF to (2) the collision efficiency and (3) the steric factor in the surface reaction model computed for Flames S1d and S3c. Symbols: experimental; lines: computed (1) base case ABF model, (2) using the size-dependent collision efficiency expression (Eq. (7)) of Ref. [18] and (3) using $a = 12.0 - 0.00563\ T$ instead of $a = 12.65 - 0.00563\ T$ in the α expression as in the ABF model.

culation (curve 1). Specifically, the particle number concentration of Flame S3c is underpredicted by as much as a factor of 100, yet the median particle diameter is still substantially over-predicted. This observation leads to the question about the surface growth reaction rate.

Appel et al. [33] proposed a temperature-dependent surface steric factor, α, to describe the reduced surface reaction rates towards high temperatures. They proposed an expression for α by fitting soot volume fraction data of eight burner-stabilized flames with $1710 < T_{f,max} < 2100$ K. The a parameter in the α expression has a high degree of scatter leading to uncertainty when extrapolated to the temperature of the current S3 flames. Subtracting 0.65 from the y-intercept of the linear (in local temperature) a parameter function has a substantial effect. A reduction of the α value by a factor of 4 to 40 depending on the average particle size, is observed even though this lower value of a still lies within the range of scatter (see the Supplemental material for additional discussion of the above points). The effect of a reduced α value is to drastically reduce particle size, as shown in Fig. 7, indicating that the reversibility may also be a critical factor in surface growth.

In light of the above sensitivity tests, we can make the following points with regard to the inability of the ABF model in reconciling the current data. First, it remains highly questionable whether available soot models can be predictive outside the conditions over which the model parameters have been determined or estimated. Second, the couplings among the various fundamental sooting processes and strong sensitivities of the PSDF to a large number of model parameters make it difficult to determine these parameters from flame data alone, without additional experiments in which the various sooting processes can be studied in an isolated manner.

4. Conclusions

Nascent soot PSDFs were measured in premixed stretch-stabilized flat flames for the first time to demonstrate that the proposed flame configuration can broaden the experimental flame condition space for studying soot formation in a pseudo-one dimensional flow configuration. The measurements show that, in agreement with previous understanding, thermodynamic reversibility towards high temperatures plays a critical role for soot formation. For the three series of flames and within the range of particle size probed, the PSDFs exhibit bimodal size distribution towards the lower end of the flame temperature (~1980 K) while they are apparently unimodal towards higher temperature flames.

Model predictions of PSDFs show reasonably good agreement with the experimental data for series S1 and S2 flames with maximum temperatures at or below 2000 K. The model over-predicted the particle number density and size for series S3 flames at ~2160 K. Sensitivity analyses suggests that a proper consideration of the thermodynamic reversibility in soot nucleation, coagulation and surface growth may be critical to predicting soot formation at temperatures greater than 2000 K.

Supplementary materials

Supplementary material associated with this article can be found, in the online version, at doi:10.1016/j.proci.2016.06.170.

References

[1] M. Frenklach, S. Taki, M. Durgaprasad, R. Matula, *Combust. Flame* 54 (1983) 81–101.
[2] H. Kellerer, R. Koch, S. Wittig, *Combust. Flame* 120 (2000) 188–199.
[3] A. Emelianov, A. Eremin, E. Gurentsov, et al., *Proc. Combust. Inst.* 30 (2005) 1433–1440.
[4] H. Böhm, D. Hesse, H. Jander, et al., *Symp. Int. Combust.* 22 (1989) 403–411.
[5] M. Bönig, C. Feldermann, H. Jander, B. Lüers, G. Rudolph, H.G. Wagner, *Symp. Int. Combust.* 23 (1991) 1581–1587.
[6] A. Ciajolo, A. D'anna, R. Barbella, A. Tregrossi, A. Violi, *Symp. Int. Combust.* 26 (1996) 2327–2333.
[7] A.D. Abid, N. Heinz, E.D. Tolmachoff, D.J. Phares, C.S. Campbell, H. Wang, *Combust. Flame* 154 (2008) 775–788.
[8] M. Frenklach, D.W. Clary, W.C. Gardiner, S.E. Stein, *Symp. Int. Combust.* 20 (1985) 887–901.
[9] M. Frenklach, *Phys. Chem. Chem. Phys.* 4 (2002) 2028–2037.
[10] H. Wang, *Proc. Combust. Inst.* 33 (2011) 41–67.
[11] A. Violi, *Combust. Flame* 139 (2004) 279–287.
[12] A. Raj, M. Sander, V. Janardhanan, M. Kraft, *Combust. Flame* 157 (2010) 523–534.
[13] M. Sander, R.I.A. Patterson, A. Braumann, A. Raj, M. Kraft, *Proc. Combust. Inst.* 33 (2011) 675–683.
[14] R. Lindstedt, B. Waldheim, *Proc. Combust. Inst.* 34 (2013) 1861–1868.
[15] N. Eaves, S. Dworkin, M. Thomson, *Proc. Combust. Inst.* 35 (2015) 1787–1794.
[16] A. D'Alessio, A. Barone, R. Cau, A. D'Anna, P. Minutolo, *Proc. Combust. Inst.* 30 (2005) 2595–2603.
[17] A. D'Anna, J. Kent, *Combust. Flame* 144 (2006) 249–260.
[18] C. Saggese, S. Ferrario, J. Camacho, et al., *Combust. Flame* 162 (2015) 3356–3369.
[19] A.D. Abid, J. Camacho, D.A. Sheen, H. Wang, *Combust. Flame* 156 (2009) 1862–1870.
[20] J. Camacho, S. Lieb, H. Wang, *Proc. Combust. Inst.* 34 (2013) 1853–1860.
[21] J. Camacho, C. Liu, C. Gu, et al., *Combust. Flame* 162 (2015) 3810–3822.
[22] C. Saggese, A. Cuoci, A. Frassoldati, S. Ferrario, J. Camacho, H. Wang, T. Faravelli, *Combust. Flame* 167 (2015) 184–197.
[23] E.K.Y. Yapp, D. Chen, J. Akroyd, et al., *Combust. Flame* 162 (2015) 2569–2581.

[24] K.V. Puduppakkam, A.U. Modak, C.V. Naik, J. Camacho, H. Wang, E. Meeks, *ASME Turbo Expo 2014: Turbine Technical Conference and Exposition* (2014) 2014; V04BT04A055.

[25] C.K. Law, *Combustion Physics*, Cambridge University Press, 2006.

[26] B. Zhao, Z. Yang, M.V. Johnston, et al., *Combust. Flame* 133 (2003) 173–188.

[27] B. Zhao, Z. Yang, J. Wang, M.V. Johnston, H. Wang, *Aerosol. Sci. Technol.* 37 (2003) 611–620.

[28] J. Singh, R.I.A. Patterson, M. Kraft, H. Wang, *Combust. Flame* 145 (2006) 117–127.

[29] Z. Li, H. Wang, *Phys. Rev. E* 68 (2003) 061207.

[30] P.-E. Danielsson, O. Seger, *Machine Vision for Three--Dimensional Scenes*, in: H. Freemen (Ed.), Adademic Press, 1990.

[31] J. Singh, M. Balthasar, M. Kraft, W. Wagner, *Proc. Combust. Inst.* 30 (2005) 1457–1465.

[32] A.E. Lutz, R.J. Kee, J.F. Grear, F.M. Rupley, OPPDIF: A FORTRAN Program for Computing Opposed-Flow Diffusion Flames, Livermore, 1997.

[33] J. Appel, H. Bockhorn, M. Frenklach, *Combust. Flame* 121 (2000) 122–136.

[34] H. Wang, M. Frenklach, *Combust. Flame* 110 (1997) 173–221.

[35] H. Wang, X. You, A.V. Joshi, et al., USC Mech Version II. High-Temperature Combustion Reaction Model of H2/CO/C1-C4 Compounds. 2007, http://ignis.usc.edu/USC_Mech_II.htm.

[36] M. Smooke, I. Puri, K. Seshadri, *Symp. Int. Combust.* 21 (1988) 1783–1792.

[37] R. Kee, J. Miller, G. Evans, G. Dixon-Lewis, *Symp. Int. Combust.* 21 (1988) 1479–1494.

[38] R.I.A. Patterson, J. Singh, M. Balthasar, M. Kraft, W. Wagner, *Combust. Flame* 145 (2006) 638–642.

[39] J. Ballester, T. García-Armingol, *Prog. Energy Combust. Sci.* 36 (2010) 375–411.

[40] J. Kojima, Y. Ikeda, T. Nakajima, *Combust. Flame* 140 (2005) 34–45.

[41] L. Waldmann, *Z. Nat. A* 14 (1959) 589–599.

[42] C. Gu, H. Lin, J. Camacho, et al., *Combust. Flame* 165 (2015) 177–187.

[43] M. Schenk, N. Hansen, H. Vieker, A. Beyer, A. Gölzhäuser, K. Kohse-Höinghaus, *Proc. Combust. Inst.* 35 (2015) 1761–1769.

[44] M. Schenk, S. Lieb, H. Vieker, et al., *Proc. Combust. Inst.* 35 (2015) 1879–1886.

[45] M. Schenk, S. Lieb, H. Vieker, et al., *ChemPhysChem* 14 (2013) 3248–3254.